Abstract

There is an urgent need of synthetic bone grafts with enhanced osteogenic capacity. This can be achieved by combining biomaterials with exogenous growth factors, which however can have numerous undesired side effects, but also by tuning the intrinsic biomaterial properties. In a previous study, we showed the synergistic effect of nanostructure and pore architecture of biomimetic calcium deficient hydroxyapatite (CDHA) scaffolds in enhancing osteoinduction, i.e. fostering the differentiation of mesenchymal stem cells to bone forming cells. This was demonstrated by assessing bone formation after implanting the scaffolds intramuscularly. The present study goes one step forward, since it analyzes the effect of the geometrical features of the same CDHA scaffolds, obtained either by 3D-printing or by foaming, on the osteogenic potential and resorption behaviour in a bony environment. After 6 and 12 weeks of intraosseous implantation, both bone formation and material degradation had been drastically affected by the macropore architecture of the scaffolds. Whereas nanostructured CDHA was shown to be highly osteoconductive both in the robocast and foamed scaffolds, a superior osteogenic capacity was observed in the foamed scaffolds, which was associated with their higher intrinsic osteoinductive potential. Moreover, they showed a significantly higher cell-mediated degradation than the robocast constructs, with a simultaneous and progressive replacement of the scaffold by new bone. In conclusion, these results demonstrate that the control of macropore architecture is a crucial parameter in the design of synthetic bone grafts, which allows fostering both material degradation and new bone formation.

Keywords: Osteogenesis; pore architecture; 3D-printing; foaming; calcium phosphate

1. Introduction

Bone has a high capacity for regeneration that is not, however, unlimited. When a bone defect exceeds a critical size, bone is not able to regenerate itself, it requires the use of a substrate, which can be natural or synthetic, to serve as a support and guide the action of bone regenerating cells [1]. While autograft is still the gold standard, the serious drawbacks associated with the need of a second surgery to harvest it and the limited availability, has prompted the search for alternatives within synthetic materials [1,2]. Calcium phosphates (CaPs) have been used since the 70s for this application. They are osteoconductive materials and perform well in many situations [2]. However, in very demanding situations they do not promote osteogenesis sufficiently. The combination of scaffolds with cells or growth factors has attracted much attention lately, although it raises ethical, logistic and economic concerns, besides suffering from poor reproducibility and patient variability [3]. An attractive alternative lies in having a deeper knowledge of the material-tissue interaction, which allows designing cell instructive biomaterials, capable of triggering the biological mechanisms behind the bone healing process.

In this context, endowing intrinsic osteoinductive properties to a synthetic bone substitute by tuning its physico-chemical and structural properties is one of the most challenging and, at the same time, promising tasks for the development of an ideal bone graft substitute that can replace autografts [4]. The design of new osteoinductive biomaterials should aim to develop biomimetic matrices that trigger the endogenous expression of osteogenic growth factors instead of adding expensive doses of exogenous growth factors [5] with the well-known associated risks [6-9]. In this regard, the control of porosity acquires major significance. Whereas open and interconnected macropores ranging from 50 to 500 μm are known to promote cell migration and vascularization, micro and nanoporosity control the interaction with proteins and modulate the ionic exchange with the extracellular fluids [2].

Although sintered CaP ceramics, including hydroxyapatite (HA), beta-tricalcium phosphate (β-TCP) and biphasic calcium phosphate (BCP), have traditionally been the most widely used synthetic bone substitutes, their biological performance is still inferior to autografts, especially in terms of initiation of bone growth and simultaneous, synchronized material resorption [4,10].

This is probably associated with the high crystallinity and lack of nanostructure of sintered ceramics, which significantly differ from the non-stoichiometric, calcium-deficient (Ca/P molar ratio lower than 1.67) and low-crystalline form of the natural bone apatite [11,12].

To overcome these limitations, biomimetic routes based on the self-setting reaction of calcium phosphate cements (CPCs) constitute an ideal platform to mimic the composition and morphology of the bone mineral phase much better than sintered ceramics, obtaining low-crystalline, non-stoichiometric and nanostructured calcium deficient hydroxyapatite (CDHA) [13]. Moreover, our group has developed processing methods to obtain scaffolds with defined macroporous architectures while preserving the biomimetic nanostructure of the CDHA, such as 3D-printing by robocasting [14,15] or foaming [16,17].

In this regard, we recently demonstrated in an *in vivo* canine study that both nanostructure and macropore geometry play a critical role in osteoinduction of CaPs [18]. Bone formation was significantly accelerated and stimulated when the scaffolds were implanted intramuscularly in the shape of nanostructured biomimetic foams compared with the high-temperature microstructured counterparts. Moreover, in agreement with other studies that have highlighted the importance of geometrical factors like curvature in bone tissue regeneration [19-21], we demonstrated that foamed scaffolds, with concave pores, induced a significantly higher amount of ectopic bone than 3D-printed scaffolds with orthogonal-shaped struts and therefore prismatic pores [18].

The present study moves one step forward, since it aims at analyzing the effect of the geometrical features of nanostructured CaPs on their osteogenic potential and resorption behaviour in a bony environment. To this end, biomimetic CDHA scaffolds, with identical chemical composition and nanostructure but different macropore geometries and dimensions were evaluated in a canine orthotopic model. We hypothesized that the high osteoinductive, spherical, concave, macroporous, foamed scaffolds (CDHA-Foam) would have a superior bone healing capacity compared with the poorly osteoinductive prismatic, convex, macroporous, robocast scaffolds (CDHA-Rob).

2. Materials and Methods

2.1 Calcium deficient hydroxyapatite scaffolds

CDHA scaffolds were prepared according to previously described methods, based on the hydrolysis of alpha-tricalcium phosphate (α-$Ca_3(PO_4)_2$, α-TCP) [18].

Briefly, α-TCP was obtained by heating calcium hydrogen phosphate ($CaHPO_4$, Sigma-Aldrich, St. Louis, MO) and calcium carbonate ($CaCO_3$, Sigma-Aldrich, St. Louis, MO) at a 2:1 molar ratio for 15 h at 1400℃ followed by quenching in air. Subsequently, the powder was milled in an agate ball mill (Pulverisette 6, Fritsch GmbB, Markt Einersheim, Germany) to a mean particle size of 2.8 µm.

The CDHA foams (CDHA-Foam) were obtained by foaming a mixture of a solid phase, consisting of 98 wt% α-TCP and 2 wt% of precipitated hydroxyapatite (PHA, Merck KGaA, Darmstadt, Germany), and an aqueous solution of 1 wt% Polysorbate 80 (Tween 80®,Sigma-Aldrich, St. Louis, MO) at a liquid to powder ratio of 0.65 mL/g using a customized hand mixer. The foam was transferred to Teflon cylindrical moulds (5 mm diameter and 10 mm height).

To obtain the robocast scaffolds, a CDHA self-setting ink was prepared containing a 30 wt% aqueous solution of poloxamer 407 (P2443 - Pluronic® F-127, Sigma-Aldrich, St. Louis, MO) and α-TCP powder, at a liquid to powder ratio of 0.65 g/g. A cylindrical CAD model of the scaffolds (5 mm diameter and 10 mm height) was designed (Solidworks 2014, Dassault Systèmes SolidWorks Corp., Waltham, MA) and converted to a STL 3D mesh, with a rectilinear pattern and an infill of 0.45. Scaffolds were printed using a robocasting device (Pastecaster, BCN3D Technologies, Barcelona, Spain) with two different nozzle diameters, 450 and 250 µm for the CDHA-Rob-450 and CDHA-Rob-250, respectively.

The transformation to CDHA, which results in the hardening of the scaffolds, was achieved by immersion of both the foams and the robocast scaffolds in deionized water at 37℃ for 10 days, to allow for the hydrolysis reaction of α-TCP, according to the following reaction (Eq.1):

$$3\ Ca_3(PO_4)_2 + H_2O \rightarrow Ca_9(PO_4)_5(HPO_4)OH \quad \text{(Eq. 1)}$$

The architecture of the foamed and 3D-printed scaffolds was determined by micro-computed tomography (micro-CT, SkyScan 1172, Bruker microCT, Kontich, Belgium) at a voltage of 90 kV

and a current of 112 µA and with a Cu–Al filter. Images were acquired using an isotropic pixel size of 5 µm. Reconstruction of cross sections was done using software package NRecon (Bruker microCT, Kontich, Belgium). Calculations of macroporosity were performed with CTAn software (Bruker microCT, Kontich, Belgium). The microstructure was characterized by scanning electron microscopy (Zeiss Neon40 EsBCrossBeam, Zeiss, Oberkochen, Germany).

The compressive strength of the different scaffolds was measured using a Universal Testing Machine (Instron 8511, Instron, Norwood, MA) at a cross-head speed of 1 mm/min until fracture.

2.2 In vivo study

2.2.1 Animal model

All animal procedures in this study were performed in compliance with the Guide for Care and Use of Laboratory Animals [22] and the European Community Guidelines (Directive 2010/63/EU) for the protection of animals used for scientific purposes [23], and under the permission of the local animal ethics committee (CEAAH 2338). The study was performed on 12 adult beagle dogs (body weight 14-17 kg) purchased from a professional stock breeder (Isoquimen S.L., Barcelona, Spain). Animals were randomly divided into 2 groups of 6 dogs each, corresponding to two different experimental times (6 or 12 weeks), and acclimatized for 2 weeks prior to surgery.

Surgical procedures were carried out under standard anesthetic and analgesic protocols, as described elsewhere [18]. For the orthotopic implantation, animals were placed in lateral recumbence and the left hind limb was clipped, scrubbed and draped for an aseptic surgery. Subsequently, the lateral aspect of the femur was approached by blunt dissection. Three round monocortical bone defects (5 mm diameter) were drilled under continuous irrigation of physiological saline and one of the above-mentioned scaffolds (5 mm diameter x 10 mm height) was inserted in each defect by press-fit. All scaffolds had previously been sterilized by gamma irradiation at a dose of 25 kG. One scaffold of each series was implanted in each dog (Table 1), the implant position being assigned according to a rotatory allocation system using a block design. The surgical wound was finally closed in layers.

Table 1. Summary of implanted scaffolds

Architecture	Codes	6 weeks	12 weeks
Foams	CDHA-Foam	6	6
Robocast	CDHA-Rob-450	6	6
	CDHA-Rob-250	6	6

Animals were allowed to full weight bearing and received a normal diet immediately after surgery. During the postoperative period, a nonsteroidal anti-inflammatory drug (NSAID), routinely used after orthopedic surgeries, was given to the animals for 7 days to prevent pain and inflammation. The animals were euthanized at 6 and 12 weeks postimplantation by an overdose of pentobarbital sodium, after sedation with medetomidine.

2.2.2 Sample harvesting and histological processing

After explantation, samples were fixed in 4% neutral buffered formalin solution for 72 h and analyzed by micro-CT. After micro-CT scanning, tissue samples were dehydrated in an increasing series of ethanol solutions and embedded in four different graded mixtures of ethanol and methyl methacrylate resin (Technovit 7200, HeraeusKulzer GmbH, Hanau, Germany) under vacuum conditions. The specimens were subsequently photopolymerized resulting in blocks, which were divided along the longitudinal axis of the implant, and transverse to the femur in order to evaluate the full thickness of the cortical bone defect. One piece was sectioned and polished (EXAKT Cutting & Grinding System, EXAKT Advanced Technologies GmbH, Norderstedt, Germany) prior to sputtering the surface with carbon for backscattered scanning electron microscopy analysis (BS-SEM). The other piece was sliced and ground (Cutting & Grinding System, EXAKT Advanced Technologies GmbH, Norderstedt, Germany) to obtain histological sections (50 µm), which were stained with Goldner-Masson trichrome and toluidine blue for histological evaluation using light microscopy.

2.2.3 Histology and histomorphometry

Micro-CT analysis (SkyScan 1172, Bruker microCT, Kontich, Belgium) of bone-tissue samples was performed as described above with the exception of an isotropic pixel size of 10 µm. The

micro-CT 3D quantification of new bone formation and scaffold degradation was performed following a previously established protocol [24], using BS-SEM images as a reference for establishing the gray-scale intensity thresholds to differentiate bone and calcium phosphate biomaterials. The following parameters were quantified:

a) Percentage of newly formed bone within the monocortical bone defect:

   % newly formed bone = (bone volume / initial available macropore volume) * 100

b) Percentage of scaffold degradation within the monocortical bone defect:

   % scaffold degradation = [(initial scaffold volume – final scaffold volume) / initial scaffold volume] * 100

Both parameters were quantified only in the monocortical bone defect volume, without considering the intramedullarly portion of the scaffold. Moreover, the radius of each scaffold was divided into three equal segments, which define three concentric volumes of interest (VOIs): outer, middle and inner VOI. The percentage of newly formed bone was calculated in each VOI, to assess the distribution of the new bone formation.

The BS-SEM observations (Zeiss Neon40 EsBCrossBeam, Zeiss, Oberkochen, Germany) were made at 20 kV to assess the localization and maturity of the newly formed bone based on morphology and the different contrast levels.

Stained histological sections were observed using a light microscope (Nikon Eclipse E800, Nikon Corp., Tokyo, Japan) fitted with a digital camera (ProgRes, Jenoptik AG, Jena, Germany) for a qualitative histological evaluation focused on the grade of peri-implant inflammatory reaction, fibrous-tissue infiltration and angiogenesis, as well as on the search for cell-mediated scaffold resorption evidences. Digital images were analyzed using an image analysis software (ProgResCapturePro, Jenoptik AG, Jena, Germany).

2.3 Statistical analysis

All results are presented as mean values ± standard error. GraphPad Prism software (GraphPad Software Inc., La Jolla, CA) was used for statistical analysis. Statistical comparisons between material characterization results were performed using Kruskal-Wallis test followed by Dunn's post hoc test. Statistic significance was defined as $p < 0.05$. Histomorphometric data were normally distributed according to Anderson-Darling and Kolmogorov-Smirnov tests.

Statistical comparisons among experimental groups were performed using one-way repeated measures ANOVA followed by Tukey's post hoc test. A pair-wise comparison result of $p < 0.05$ was considered statistically significant.

3. Results

3.1. Materials characterization

The micro-CT reconstructions of the different scaffolds, as well as the nanostructures observed by SEM are shown in Figure 1A. Similar nanostructures were observed for the CDHA-Foam, CDHA-Rob-450 and CDHA-Rob-250 with the typical entangled network of needle-like CDHA nanocrystals, which resulted in high specific surface areas (SSA) (Figure 1B) [18], with no statistically significant differences between samples ($p > 0.05$). All scaffolds presented similar porosity and macroporosity ($p > 0.05$), although different pore sizes and, more markedly, different pore entrance sizes, which were larger for the robocast scaffolds, as determined in a previous study and summarized in Figure 1B [18]. Moreover, similar compression strength values (around 5 MPa) were found for all scaffolds irrespective of their architecture (foamed vs. robocast) and the strand diameter in the robocast constructs (Figure 1C), with no statistically significant differences between series ($p > 0.05$).

3.2. *In vivo* results

Surgeries were uneventful and all animals completed a normal postoperative period without any clinical complication. All implanted scaffolds were retrieved and processed for histological evaluation. Histology showed mild peri-implant inflammatory reactions at both time points for all scaffolds. The cortical bone tissue became closely connected to all three types of scaffolds and no fibrous capsules were observed at the host cortical bone-material interfaces (Figure 2A,B and C). All scaffolds showed a certain degree of loose fibrous-tissue infiltration within interconnected macropores, minimal in the foams and more pronounced in the robocast scaffolds, especially in the central areas of the defects (Figure 2D,E,F). A rich widespread blood vessel network was found in the macropores of all three groups, from small capillaries to

medium size vessels, as shown in the Goldner-Masson-trichrome-stained sections (Figure 2G,H,I).

The morphology of newly deposited bone, which consisted of a mix of woven bone and some areas of well organized lamellar bone following a Haversian pattern, was also similar for all groups (Supplementary Material, Figure S1). The main finding, however, was that CDHA-Foams promoted a higher penetration of the cortical bone, with new bone present in the centre of the scaffold already at 6 weeks, in contrast to the robocast scaffolds in which at this time point the new bone was penetrating into the scaffold only from the margin of the defect (Figure 3).

These histological findings were confirmed by the histomorphometric results, summarized in Figure 4. At 6 weeks the percentage of newly formed bone was significantly higher in the CDHA-Foam group than in the robocast groups (Figure 4A). Regarding bone distribution within the scaffolds (Figure 4B), the percentage of newly formed bone at 6 weeks was superior in all three VOIs for the foamed scaffolds compared with the robocast counterparts (Figure 4C). The main difference was that small amounts of bone were detected in the robocast scaffolds within the middle and, especially, within the inner VOIs, whereas in the foamed scaffolds bone distribution was more homogeneous (Figure 4C).

The same trend was observed at 12 weeks, with newly formed bone increasing both in quantity and maturity for all groups (Figures 4A and 5). CDHA-Foams showed a full-thickness cortical bone bridging while some gaps were still observed in the central regions of the bone defects in most robocast scaffolds (Figure 5). The histomorphometrical results showed a significantly larger amount of newly formed bone in the CDHA-Foam group than in CDHA-Rob-450 and CDHA-Rob-250 groups (Figure 4A). No significant differences were found between the two robocast groups despite the different macropore sizes, similarly to what happened at 6 weeks. Bone distribution between the inner, middle and outer VOIs was more homogeneous than it was at 6 weeks for all scaffolds, including the robocast ones (Figures 4D).

Additionally, new bone formation was observed also in the intramedullary portion of the scaffold in the case of CDHA-Foam, while no bone was observed in the robocast scaffolds, as shown in Figure 6.

The micro-CT quantitative analysis of scaffold degradation is summarized in Figure 7A. A significantly higher degradation was found for the CDHA-Foams compared with the robocast scaffolds at 12 weeks postimplantation, while no significant differences were found at 6 weeks. The resorption of robocast scaffolds did not progress among the 6 and 12 week time point (Figure 7A). Histological images showed that both foamed and robocast scaffolds sustained cell-mediated degradation as revealed by the presence of cutting cones in close contact with the materials and the consistent observation of multinucleated osteoclast-like cells eroding the materials in all groups (Figure 7B). Morphologies compatible with typical Howship's Lacunae were clearly observed in the three scaffolds, as shown in Figure 7B. A greater amount of osteoclast-like cells were observed in the CDHA-Foams than in the robocast samples, especially 12 weeks after implantation.

4. Discussion

The aim of the present study was to assess the relevance of macropore geometry in the osteogenic potential and degradation of nanostructured biomimetic CaP scaffolds. The interest of these materials was highlighted in a previous study [18], in which we demonstrated a synergistic effect between nanostructure and pore architecture with regards to osteoinduction, i.e, the capacity to produce bone in a non-osseous environment, which is associated with the differentiation of progenitor cells to the osteogenic lineage. Therein, nanostructured CDHA-Foams, with concave macropores, exhibited an accelerated and enhanced osteoinduction when compared with nanostructured 3D-printed CDHA scaffolds (CDHA-Rob) [18]. The correlation between the intrinsic osteoinduction and the osteogenic potential in an osseous environment was also the subject of the present study.

4.1 Biocompatibility and Angiogenesis

The histological evaluation of the samples showed the host cortical bone directly connected to all scaffolds with no evidence of fibrous encapsulation neither foreign body reaction (Figure 2A,B,C), which confirmed the good biocompatibility of the CDHA-based biomaterials, as observed in previous ectopic [18,25] and orthotopic [12,25-31] studies.

However, a certain degree of loose fibrous-tissue infiltration, coming from the soft tissues in contact with the external surface of the scaffold was observed in all groups since guided bone regeneration membranes were not used to protect the bone defect from soft tissue invasion. It is worth mentioning, however, that fibrous-tissue infiltration was significantly more extensive within the central macropores of the robocast samples than that observed in the foams (Figure 2D,E,F). This finding can probably be associated with the linear geometry and larger macropore entrance size of these scaffolds (Figure 1B) compared with the foamed scaffolds, and suggests that the smaller pore entrance size of the CDHA-Foam scaffolds (70 µm) together with their more tortuous morphology prevent fibrous tissue colonization into the bone defect guiding the bone healing more effectively. This could partly explain the lower values of newly formed bone and, especially, the lack of new bone formation in the central regions of the robocast scaffolds compared with the CDHA-Foam group at 6 weeks.

Abundant neovascularization was found, homogeneously distributed within the macropores of all three scaffolds (Figure 2G,H,I), enabled by the open and highly interconnected macroporosity both in the foamed and the robocast scaffolds. Angiogenesis is in fact one of the top priorities in bone tissue engineering, since it provides oxygen and nutrient supply to the bone forming cells, it represents the main access pathway of cells (inflammatory cells, stem cells) and soluble proteins (signalling molecules and osteogenic growth factors), and it is a source of undifferentiated cells called vascular pericytes, that can potentially differentiate into osteogenic lineage cells [5,10].

4.2 Effect of macropore architecture on osteoinduction and osteoconduction

The histomorphometrical results showed a significantly higher percentage of new bone formation in the CDHA-Foams than in the robocast scaffolds at both time points (Figure 4A). Considering that the foamed and the robocast scaffolds shared the same chemical composition (CDHA), a similar percentage of total porosity (around 70%), a similar nanostructure (needle-like crystals) and a similar SSA (around 35 g/m^2) (Figure 1), the differences observed in their bone healing capacity can be attributed to the different macropore architectures (Figure 1A).

It is worth noting that, while abundant bone ingrowth was observed in the outer VOI in all three groups, proving excellent osteoconductive properties, very small amounts of bone were detected in the central macropores of the robocast scaffolds at 6 weeks (Figure 3 and Figure 4C). However, a significant amount of new bone was observed in the central areas of the CDHA-Foams at this time point (Figure 3 and Figure 4C). Likewise, new bone was found within the central macropores of the intramedullary portion of CDHA-Foams (Figure 6A), far from the host cortical bone regeneration front, whereas no bone was observed within the prismatic macropores of the intramedullary portion of robocast scaffolds (Figure 6B). Although, it cannot be ruled out that the better performance of foamed scaffolds could derive from an increased osteoconductive capacity, the higher osteoinductive potential demonstrated previously [18] for the foamed scaffolds compared with the robocast scaffolds suggest that osteoinduction could be the underlying mechanism of bone formation in these specific sites. The osteoinductive phenomena, thus, would contribute directly to the higher osteogenesis of the CDHA-Foams when implanted in a bony site. A similar correlation between osteoinduction and osteogenic capacity was previously reported by other authors evaluating sintered ceramics [32-35].

Although the same trend was observed at 12 weeks, the differences among the outer VOI versus the middle and inner VOIs in the robocast scaffolds were less pronounced than those observed at 6 weeks (Figure 4C/D), probably because the high osteoconductivity of the robocast scaffolds compensated for the lack of osteoinductive capacity, highlighting the contribution of both osteoconduction and osteoinduction in the total bone formation.

Regarding the role of pore geometry on bone formation, our results seem to be in contradiction with previous studies that reported better bone healing capacities for scaffolds with prismatic macropores with convex [36] or flat [37] surfaces, obtained by rapid prototyping techniques (robocasting and microstereolithography) than for constructs with spherical macropores with concave surfaces obtained by conventional processing methods like salt leaching or gas foaming processes [36,37]. However, in both orthotopic studies the authors attributed the lower bone healing capacity of the scaffolds with concave macropores to their limited interconnectivity, and consequently their lower osteoconductive potential. Therefore, the different macropore interconnectivity and the lack of characterization of other parameters such as microstructure

and the surface topography in those studies prevented the identification of the real role of macropore geometry on the osteogenic capacity of these scaffolds.

Regarding the role of pore size on bone healing capacity, it is difficult to compare foamed and robocast scaffolds due to the different pore geometry. Whereas in the foams pore entrance size is much smaller than pore size (bottle neck effect), this is not the case in robocast scaffolds. When comparing CDHA-Rob-450 and CDHA-Rob-250, which had different pore sizes, no differences were found in terms of the amount and distribution of newly formed bone. In accordance to these findings, some authors reported bone ingrowth in 3D-printed scaffolds with pore sizes in the same range to the ones tested in the present study to be largely independent of the rod diameter [38,39] and the distance between rods [38].

4.3 Effect of macropore architecture on scaffold resorption and osteoclastogenesis

Pore architecture also had a significant effect on the degradation of the biomimetic scaffolds. CDHA-Foams underwent a four times greater degradation than the biomimetic robocast scaffolds after 12 weeks of implantation (Figure 7A), which was in line with the previous study where the same scaffolds were implanted intramuscularly [18]. In contrast, no differences were found at 6 weeks between the degradation of the foams and the robocast scaffolds implanted intraosseoulsy, whereas intramuscularly the degradation of the foams was higher than that of the robocast scaffolds [18]. This could be ascribed to differences in the inflammatory cascade and the consequent cellular environment, as well as the different mechanical stimuli in each tissue. Interestingly, however, both ectopically and orthotopically the degradation of the robocast scaffolds remained low after 12 weeks of implantation [18]. The high degradation rate of the CDHA-Foams was coupled with a high osteogenic potential, allowing a synchronization that led to the progressive replacement of the scaffold by new bone (Figure 5 and 6). This explains why at 12 weeks the percentage of newly formed bone within the initial macropore volume was over a hundred per cent (Figure 4A), since the final macropore volume was larger than the initial macropore volume and it was almost completely filled with new bone. Conversely, the new bone in the robocast scaffolds was deposited on the surface of the scaffold struts, with limited degradation, which did not increase between 6 and 12 weeks (Figure 5).

The fact that the physiological fluid is supersaturated with respect to CDHA, together with the presence of cutting cones in close contact with the scaffolds and the consistent observation of multinucleated osteoclast-like cells eroding the materials in all groups point to a cell-mediated degradation rather than a passive degradation (chemical physiologic dissolution), which is in agreement with previous *in vivo* studies with CDHA-based biomaterials [18,25-28,31]. Moreover, it is worth highlighting that the histological assessment identified a higher number of osteoclast-like cells in the concavities of the CDHA-Foams compared to the prismatic convex macropores of the robocast scaffolds. These results are again in agreement with the previous ectopic implantation study [18] and demonstrate that osteoclast-like cells activity and consequently, the degradation rate, are strongly influenced by the geometry of the macropores.

The superior osteoclast activity observed in the CDHA-Foams could also be an explanation for their superior osteoinductive potential and, hence, the superior bone healing capacity compared with the robocast scaffolds. The active involvement of osteoclasts in osteoinduction has been demonstrated in previous studies by the reduced ectopic bone formation and a decreased BMP expression by osteoinductive CaP biomaterials when treated with bisphosphonate, an osteoclast inhibitor [40-42].

The fostering of bone formation by CDHA-Foams can, therefore, be associated with the concave macropores, with small entrance sizes and nanostructured walls, which provide the adequate microenvironment that may act as a powerful attractant for macrophages and trigger osteoclastogenesis. In turn, the retention within this volume of both osteogenic growth factors secreted by active osteoclasts (BMPS, Wnts, S1P, OSM, PDGF-BB and CTHRC1) [42-48] and calcium and phosphate ions resulting from the osteoclastic resorption of CaP materials [49-54] are known to trigger not only the activity of osteoblasts but also the differentiation of mesenchymal stem cells into bone-forming cells, leading eventually to *de novo* bone formation.

The results obtained in this study, far from going against 3D printing, a technology that enables the fast fabrication of patient-specific complex bone grafts, stress the importance of pushing the enormous possibilities of this technique in the right direction. Its great versatility allows exerting a superior control of the architecture of the constructs that are obtained. It is important to take advantage of this feature to design the right pore geometry, looking for concave surfaces that

allow having the optimum microenvironment to trigger the bone healing mechanisms. While in the present work we chose the simplest pattern with orthogonal struts, the osteogenic potential of other patterns, with more complex internal geometries should be assessed in future studies.

5. Conclusions

Pore geometry plays a crucial role in the *in vivo* performance of biomimetic CDHA-based bone substitutes. Both bone formation and material degradation of chemically identical materials with the same nanostructure and similar pore volumes were drastically affected by the macropore architecture of the scaffolds. Whereas CDHA was highly osteoconductive both in the robocast and foamed scaffolds, the superior bone healing capacity of the foamed scaffolds with spherical concave macropores correlated well with their higher intrinsic osteoinductive potential. The contribution of both osteoconduction and osteoinduction accelerated the complete healing of the bone defects. Moreover, the foamed scaffolds showed a superior resorption to the robocast constructs, triggering the simultaneous and progressive scaffold replacement by new bone. The different macropore size between the two robocast scaffolds did not have a significant effect neither on new bone formation nor on degradation. Overall, the high osteogenic potential of this new family of biomimetic nanostructured CDHA foams makes them a very attractive alternative, safer and more affordable than the use of exogenous growth factors and cell-based therapies. The next step towards the clinical application would be to test its efficacy in a large segmental bone defect.

6. Acknowledgments

This work was supported by the Spanish Government [MAT2015-65601-R Project], co-funded by the EU through European Regional Development Funds; and the Swedish Foundation for International Cooperation in Research and Higher Education [STINT, GA IG2011-2047]. The authors thank also the Generalitat the Catalunya for funding through project 2017SGR-1165. MPG acknowledges the ICREA Academia award and ME the Serra Hunter Fellowship, both from the Generalitat de Catalunya. AB acknowledges a FPU scholarship from the Spanish Ministry of Education. Authors are grateful to Eva Sanchez from Pathology and Experimental

Therapeutics Department at Universitat de Barcelona for her technical assistance with histology, Dr. Trifon Trifonov from Barcelona Research Center in Multiscale Science and Engineering at Universitat Politècnica de Catalunya for his technical assistance with BS-SEM analysis and Susanne Lewin from Materials in Medicine Group at Uppsala University for her technical assistance with micro-CT analysis.

7. References

[1] P.V. Giannoudis, H. Dinopoulos, E. Tsiridis, Bone substitutes: an update, Injury 36 (2005) 20-27.

[2] G. Hannink, J.J. Arts, Bioresorbability, porosity and mechanical strength of bone substitutes: what is optimal for bone regeneration?, Injury 42 (2011) S22-25.

[3] W. Habraken, P. Habibovic, M. Epple, M. Bohner, Calcium phosphates in biomedical applications: materials for the future?, Mater. Today 19 (2016) 69-87.

[4] P. Habibovic, Strategic directions in osteoinduction and biomimetics, Tissue Eng. Part A 23 (2017) 1295-1296.

[5] U. Ripamonti, L.C. Roden, C. Ferretti, R.M. Klar, Biomimetic matrices self-initiating the induction of bone formation, J. Craniofac. Surg. 22 (2011) 1859-1870.

[6] K.R. Garrison, S. Donell, J. Ryder, I. Shemilt, M. Mugford, I. Harvey, F. Song, Clinical effectiveness and cost-effectiveness of bone morphogenetic proteins in the non-healing of fractures and spinal fusion: a systematic review, Health Technol. Asses. 11 (2007) 1-150.

[7] L.B. Shields, G.H. Raque, S.D. Glassman, M. Campbell, T. Vitaz, J. Harpring, C.B. Shields, Adverse effects associated with high-dose recombinant human bone morphogenetic protein-2 use in anterior cervical spine fusion, Spine (Phila Pa 1976) 31 (2006) 542-547.

[8] E. Argintar, S. Edwards, J. Delaha, Bone morphogenetic proteins in orthopaedic trauma surgery, Injury 42 (2011) 730-734.

[9] J.N. Zara, R.K. Siu, X. Zhang, J. Shen, R. Ngo, M. Lee, W. Li, M. Chiang, J. Chung, J. Kwak, B.M. Wu, K. Ting, C. Soo, C. High doses of bone morphogenetic protein 2 induce

structurally abnormal bone and inflammation in vivo, Tissue Eng. Part A 17 (2011) 1389-1399.

[10] A.M.C. Barradas, H. Yuan, C.A. van Blitterswijk, P. Habibovic, Osteoinductive biomaterials: current knowledge of properties, experimental models and biological mechanisms, Eur. Cell. Mater. 21 (2011) 407-429.

[11] B. Wopenka, J.D. Pasteris, A mineralogical perspective on the apatite in bone, Mater. Sci. Eng. C 25 (2005) 131-143.

[12] P. Sponer, M. Strnadová, K. Urban, In vivo behaviour of low-temperature calcium-deficient hydroxyapatite: comparison with deproteinised bovine bone, Int. Orthop. 35 (2011) 1553-1560.

[13] M.P. Ginebra, M. Espanol, E.B. Montufar, R.A. Perez, G. Mestres, New processing approaches in calcium phosphate cements and their applications in regenerative medicine, Acta Biomater. 6 (2010) 2863-2873.

[14] Y. Maazouz, E.B. Montufar, J. Guillem-Marti, I. Fleps, C. Öhman, C. Persson, M.P. Ginebra, Robocasting of biomimetic hydroxyapatite scaffolds using self-setting inks, J. Mater. Chem. B 2 (2014) 5378-5386.

[15] Y. Maazouz, E.B. Montufar, J. Malbert, M. Espanol, M.P. Ginebra, Self-hardening and thermoresponsive alpha tricalcium phosphate/pluronic pastes, Acta Biomater. 49 (2017) 563-574.

[16] E.B. Montufar, T. Traykova, C. Gil, I. Harr, A. Almirall, A. Aguirre, E. Engel, J.A. Planell, M.P. Ginebra, Foamed surfactant solution as a template for self-setting injectable hydroxyapatite scaffolds for bone regeneration, Acta Biomater. 6 (2010) 876-885.

[17] D. Pastorino, C. Canal, M.P. Ginebra, Drug delivery from injectable calcium phosphate foams by tailoring the macroporosity-drug interaction, Acta Biomater. 12 (2015) 250-259.

[18] A. Barba, A. Diez-Escudero, Y. Maazouz, K. Rappe, M. Espanol, E.B. Montufar, M. Bonany, J.M. Sadowska, J. Guillem-Marti, C. Öhman-Mägi, C. Persson, M.C. Manzanares J. Franch, M.P. Ginebra, Osteoinduction by foamed and 3D-printed calcium phosphate scaffolds: effect of nanostructure and pore architecture, ACS Appl. Mater. Interfaces 9 (2017) 41722-41736.

[19] U. Ripamonti, J. Crooks, A.N. Kirkbride, Sintered porous hydroxyapatites with intrinsic osteoinductive activity: geometric induction of bone formation. S. Afr. J. Sci. 95 (1999) 335-343.

[20] C.M. Bidan, K.P. Kommareddy, M. Rumpler, P. Kollmannsberger, Y.J. Bréchet, P. Fratzl, J.W. Dunlop, How linear tension converts to curvature: geometric control of bone tissue growth, PLoS One 7 (2012) e36336.

[21] C.M. Bidan, K.P. Kommareddy, M. Rumpler, P. Kollmannsberger, P. Fratzl, J.W. Dunlop, Geometry as a factor for tissue growth: towards shape optimization of tissue engineering scaffolds. Adv. Healthc. Mater. 2 (2013) 186-194.

[22] National Research Council. Guide for the Care and Use of Laboratory Animals; National Academy Press: Washington, DC, 1996; pp 41-194.

[23] Directive 2010/63/EU of the European Parliament and of the Council of 22 September 2010 on the Protection of Animals Used for Scientific Purposes. Available at http://data.europa.eu/eli/dir/2010/63/oj.

[24] S. Lewin, A. Barba, C. Persson, J Franch, M.P. Ginebra, C. Öhman-Mägi, Evaluation of bone formation in calcium phosphate scaffolds with mCT – Method validation using SEM, Biomed. Mater. 12 (2017) 65005.

[25] H. Yuan, Y. Li, J.D. de Bruijn, K. de Groot, X. Zhang, Tissue responses of calcium phosphate cement: a study in dogs, Biomaterials 21 (2000) 1283-1290.

[26] B. Bourgeois, O. Laboux, L. Obadia, O. Gauthier, E. Betti, E. Aguado, G. Daculsi, J.M. Bouler, Calcium-deficient apatite: a first in vivo study concerning bone ingrowth, J. Biomed. Mater. Res. A 65 (2003) 402-408.

[27] T. Okuda, K. Ioku, I. Yonezawa, H. Minagi, Y. Gonda, G. Kawachi, M. Kamitakahara, Y. Shibata, H. Murayama, H. Kurosawa, T. Ikeda, The slow resorption with replacement by bone of a hydrothermally synthesized pure calcium-deficient hydroxyapatite, Biomaterials 29 (2008) 2719-2728.

[28] Y. Gonda, K. Ioku, Y. Shibata, T. Okuda, G. Kawachi, M. Kamitakahara, H Murayama, K. Hideshima, S. Kamihira, I. Yonezawa, H. Kurosawa, T. Ikeda, Stimulatory effect of hydrothermally synthesized biodegradable hydroxyapatite granules on osteogenesis and direct association with osteoclasts, Biomaterials 30 (2009) 4390-4400.

[29] H. Guo, J. Su, J. Wei, H. Kong, C. Liu, Biocompatibility and osteogenicity of degradable Ca-deficient hydroxyapatite scaffolds from calcium phosphate cement for bone tissue engineering, Acta Biomater. 5 (2009) 268-278.

[30] L. Ambrosio, V. Guarino, V. Sanginario, P. Torricelli, M. Fini, M.P. Ginebra, J.A. Planell R. Giardino, Injectable calcium-phosphate-based composites for skeletal bone treatments, Biomed. Mater. 7 (2012) 024113.

[31] E. Cuzmar, R.A. Perez, M.C. Manzanares, M.P. Ginebra, J. Franch, In vivo osteogenic potential of biomimetic hydroxyapatite/collagen microspheres: comparison with injectable cement pastes, PLoS One 10 (2015) e0131188.

[32] H. Yuan, C.A. van Blitterswijk, K. de Groot, J.D. de Bruijn, A comparison of bone formation in biphasic calcium phosphate (BCP) and hydroxyapatite (HA) implanted in muscle and bone of dogs at different time periods, J. Biomed. Mater. Res. A 78 (2006) 139-147.

[33] P. Habibovic, H. Yuan, M. van den Doel, T.M. Sees, C.A. van Blitterswijk, K. de Groot, Relevance of osteoinductive biomaterials in critical-sized orthotopic defect, J. Orthop. Res. 24 (2006) 867-876.

[34] H. Yuan, H. Fernandes, P. Habibovic, J. de Boer, A.M.C. Barradas, A. de Ruiter, W.R. Walsh, C.A. van Blitterswijk, J.D. de Bruijn, Osteoinductive ceramics as a synthetic alternative to autologous bone grafting, Proc. Natl. Acad. Sci. U.S.A. 107 (2010) 13614-13619.

[35] P. Habibovic, M.V. Juhl, S. Clyens, R. Martinetti, L. Dolcini, N. Theilgaard, C.A. van Blitterswijk, Comparison of two carbonated apatite ceramics in vivo, Acta Biomater. 6 (2010) 2219-2226.

[36] S.J. Heo, S.E. Kim, J. Wei, D.H. Kim, Y.T. Hyun, H.S. Yun, H.K. Kim, T.R. Yoon, S.H. Kim, S.A. Park, J.W. Shin, In vitro and animal study of novel nano-hydroxyapatite/poly(epsilon-caprolactone) composite scaffolds fabricated by layer manufacturing process, Tissue Eng. Part A 15 (2009) 977-989.

[37] Y.J. Seol, J.Y. Park, J.W. Jung, J. Jang, R. Girdhari, S.W. Kim, D.W. Cho, Improvement of bone regeneration capability of ceramic scaffolds by accelerated release of their calcium ions, Tissue Eng. Part A 20 (2014) 2840-2849.

[38] J.L. Simon, S. Michna, J.A. Lewis, E.D. Rekow, V.P. Thompson, J.E. Smay, A. Yampolsky, J.R. Parsons, J.L. Ricci, In vivo bone response to 3D periodic hydroxyapatite scaffolds assembled by direct ink writing, J. Biomed. Mater. Res. A 83 (2007) 747-758.

[39] K.F. Lin, S. He, Y. Song, C.M. Wang, Y. Gao, J.Q. Li, P. Tang, Z. Wang, L. Bi, G.X. Pei, Low-temperature additive manufacturing of biomimic three-dimensional hydroxyapatite/collagen scaffolds for bone regeneration, ACS Appl. Mater. Interfaces 8 (2016) 6905-6916.

[40] U. Ripamonti, R.M. Klar, L.F. Renton, C. Ferretti, Synergistic induction of bone formation by Hop-1, Htgf-beta3 and inhibition by zoledronate in macroporous coral-derived hydroxyapatites, Biomaterials 31 (2010) 6400-6410.

[41] R.M. Klar, R. Duarte, T. Dix-Peek, C. Dickens, C. Ferretti, U. Ripamonti, Calcium ions and osteoclastogenesis initiate the induction of bone formation by coral-derived macroporous constructs, J. Cell. Mol. Med. 17 (2013) 1444-1457.

[42] N.L. Davison, A.L. Gamblin, P. Layrolle, H. Yuan, J.D. de Bruijn, F. Barrère-de Groot, Liposomal clodronate inhibition of osteoclastogenesis and osteoinduction by submicrostructured beta-tricalcium phosphate, Biomaterials 35 (2014) 5088-5097.

[43] R. Garimella, S.E. Tague, J. Zhang, F. Belibi, N. Nahar, B.H. Sun, K. Insogna, J. Wang, H.C. Anderson, Expression and synthesis of bone morphogenetic proteins by osteoclasts: a possible path to anabolic bone remodeling, J. Histochem. Cytochem. 56 (2008) 569-577.

[44] L Pederson, M. Ruan, J.J. Westendorf, S. Khosla, M.J. Oursler, Regulation of bone formation by osteoclasts involves Wnt/BMP signaling and the chemokine Sphingosine-1-phosphate, Proc. Natl. Acad. Sci. U.S.A. 105 (2008) 20764-20769.

[45] L. Kreja, R.E. Brenner, A. Tautzenberger, A. Liedert, B. Friemert, C. Ehrnthaller, M. Huber-Lang, A. Ignatius, Non-resorbing osteoclasts induce migration and osteogenic differentiation of mesenchymal stem cells, J. Cell. Biochem. 109 (2010) 347-355.

[46] N. Akiyama, M. Takemoto, F. Fujibayashi, M. Neo, M. Hirano, T. Nakamura, Difference between dogs and rats with regard to osteoclast-like cells in calcium-deficient hydroxyapatite-induced osteoinduction, J. Biomed. Mater. Res. A 96 (2011) 402-412.

[47] S. Takeshita, T. Fumoto, K. Matsuoka, K. Park, H. Aburatani, S. Kato, M. Ito, K. Ikeda, Osteoclast-secreted CTHRC1 in the coupling of bone resorption to formation, J. Clin. Invest. 123 (2013) 3914-3924.

[48] N.L. Davison, J. Su, H. Yuan, J.J. van den Beucken, J.D. de Bruijn, F. Barrère-de Groot, Influence of surface microstructure and chemistry on osteoinduction and osteoclastogenesis by biphasic calcium phosphate discs, Eur. Cell. Mater. 29 (2015) 314-329.

[49] G.R. Beck Jr, Inorganic phosphate as a signaling molecule in osteoblast differentiation, J. Cell. Biochem. 90 (2003) 234-243.

[50] M.M. Dvorak, D. Riccardi, Ca^{2+} as an extracellular signal in bone, Cell Calcium 35 (2004) 249-255.

[51] N. Kondo, A. Ogose, K. Tokunaga, H. Umezu, K. Arai, N. Kudo, M. Hoshino, H. Inoue, H. Irie, K. Kuroda, H. Mera, N. Endo, Osteoinduction with highly purified beta-tricalcium phosphate in dog dorsal muscles and the proliferation of osteoclasts before heterotopic bone formation, Biomaterials 27 (2006) 4419-4427.

[52] M. Zayzafoon, Calcium/calmodulin signaling controls osteoblast growth and differentiation, J. Cell. Biochem. 97 (2006) 56-70.

[53] P. Habibovic, D.C. Bassett, C.J. Doillon, C. Gerard, M.D. McKee, J.E. Barralet, Collagen biomineralization in vivo by sustained release of inorganic phosphate ions, Adv. Mater. 22 (2010) 1858-1862.

[54] A.M.C. Barradas, H.A.M. Fernandes, N. Groen, Y.C. Chai, J. Schrooten, J. van de Peppel, J.P. van Leeuwen, C.A. van Blitterswijk, J. de Boer, A calcium-induced signaling cascade leading to osteogenic differentiation of human bone marrow-derived mesenchymal stromal cells, Biomaterials 33 (2012) 3205-1325.

Figure Legends

Figure 1. (A1,A2,A3) Micro-CT 3D reconstructions of the three implanted materials showing the different macropore shapes and sizes. Note the open and interconnected, spherical, concave macropores of different sizes in the CDHA-Foam group, whereas both robocast scaffolds present open and interconnected, prismatic, convex macropores with different strand diameters between groups and, hence, different pore sizes. (A4,A5,A6) Scanning electron micrographs of the three implanted materials showing similar nanostructures for all groups with the typical entangled network of needle-like CDHA nanocrystals. (B) Textural properties of the three implanted scaffolds: total porosity and macroporosity determined by mercury intrusion porosimetry (MIP), macroporosity measured by micro-CT, average entrance size of the macropores by MIP, average macropore size measured by micro-CT and specific surface area (SSA) determined by nitrogen adsorption [18]. (C) Compressive strength of the studied scaffolds. (*) denotes no statistically significant differences between materials ($p > 0.05$, n=4).

Figure 2. Micrographs of undecalcified sections of CDHA-Foam, CDHA-Rob-450 and CDHA-Rob-250 scaffolds after 6 weeks of implantation. (A,B,C) Toluidine-blue-stained sections showing the absence of fibrous-tissue interposition between the host cortical bone (HB) and material (M) in all three groups. Note the formation of well-mineralized bone matrix (asterisks) in close contact to all three materials. (D,E,F) Toluidine-blue-stained sections showing loose fibrous-tissue (FT) infiltration in the central regions of both robocast scaffolds, whereas no fibrous-tissue was detected within the macropores of the same region in the foams. M is material, and asterisks denote calcified bone matrix. (G,H,I) Goldner-Masson-trichrome-stained sections showing a rich widespread blood vessel (black arrows) network within the macropores of all three scaffolds. M is material, and asterisks denote calcified bone matrix.

Figure 3. Micro-CT 3D images and BS-SEM micrographs of the different scaffolds after 6 weeks of implantation. (A) Micro-CT 3D reconstruction, (B) Micro-CT section and (C) BS-SEM micrograph of a CDHA-Foam scaffold. Note the presence of newly formed bone in direct contact to the concave surfaces of spherical macropores in the centre of the defect aside from the centripetal new bone formation coming from the margins of the cortical defect. (D) Micro-CT 3D reconstruction, (E) Micro-CT section and (F) BS-SEM micrograph of a CDHA-Rob-450 scaffold. (G) Micro-CT 3D reconstruction, (H) Micro-CT section, and (I) BS-SEM micrograph of a CDHA-Rob-250 scaffold. Note the absence of new bone in the central region of the defect in the two robocast scaffolds, in which the newly formed bone is restricted to the peripheral areas of the scaffold, in the edges of the cortical defect.

Figure 4. (A) Histomorphometrical results: percentage of newly formed bone within the monocortical bone defect at 6 and 12 weeks postimplantation, as measured by micro-CT. (*) denotes groups with statistically significant differences at the same time point ($p < 0.05$). (B) Diagram of the three volumes of interest (VOIs). The radius of each implanted scaffold was divided into three equal segments, which define three concentric VOIs: outer, middle and inner VOI. (C) Histomorphometrical results: percentage of newly formed bone within the three VOIs 6 weeks after implantation. Small amounts of bone were detected in the middle and inner VOIs in both robocast scaffolds, whereas in the foamed scaffolds bone distribution was more homogeneous, regardless of the VOIs. (D) Histomorphometrical results: percentage of newly formed bone within the three VOIs after 12 weeks of implantation.

Figure 5. Micro-CT 3D images and BS-SEM micrographs of the different scaffolds after 12 weeks of implantation. (A) Micro-CT 3D reconstruction, (B) Micro-CT section and (C) BS-SEM micrograph of a CDHA-Foam scaffold showing a full-thickness cortical bone bridging and a significant resorption of the scaffold. (D) Micro-CT 3D reconstruction, (E) Micro-CT section and (F) BS-SEM micrograph of a CDHA-Rob-450 scaffold. Note the gap in the central region of the cortical defect. (G) Micro-CT 3D reconstruction, (H) Micro-CT section and (I) BS-SEM micrograph of a CDHA-Rob-250 scaffold showing the incomplete bone bridging after 12 weeks of implantation.

Figure 6. BS-SEM micrographs of a CDHA-Foam scaffold (A) and of a CDHA-Rob-250 (B) after 12 weeks of implantation. Note the presence of new bone formation in close contact to the concave surfaces of the central macropores in the intramedullary portion of the foamed scaffold (C), whereas no bone is observed within the central macropores of the same region in the robocast scaffold (D).

Figure 7. Scaffold degradation. (A) Histomorphometry results: percentage of scaffold degradation after 6 and 12 weeks of implantation. Groups identified by the same superscripts are not statistically different ($P > 0.05$). Letters indicate differences between materials at each time point, numbers identify differences between time points within the same material ($P < 0.05$). (B) Micrographs of undecalcified toluidine-blue-stained sections after 12 weeks of implantation of studied scaffolds: (B1) CDHA-Foam, (B2) CDHA-Rob-450, (B3) CDHA-Rob-250. Note the presence of the typical resorption pits (black arrow heads) in the material surfaces, known as Howship's Lacunae, eroded by active multinucleated osteoclast-like cells (black arrows) in all three groups, being more numerous in the CDHA-Foam. M is material, and asterisks denote calcified bone matrix.

Statement of Significance

3D-printing technologies open new perspectives for the design of patient-specific bone grafts, since they allow customizing the external shape together with the internal architecture of implants. In this respect, it is important to design the appropriate pore geometry to maximize the bone healing capacity of these implants. The present study analyses the effect of pore architecture of nanostructured hydroxyapatite scaffolds, obtained either by 3D-printing or foaming, on the osteogenic potential and scaffold resorption in an *in vivo* model. While nanostructured hydroxyapatite showed excellent osteoconductive properties irrespective of pore geometry, we demonstrated that the spherical, concave macropores of foamed scaffolds significantly promoted both material resorption and bone regeneration compared to the 3D-printed scaffolds with orthogonal-patterned struts and therefore prismatic, convex macropores.

Figure(s)

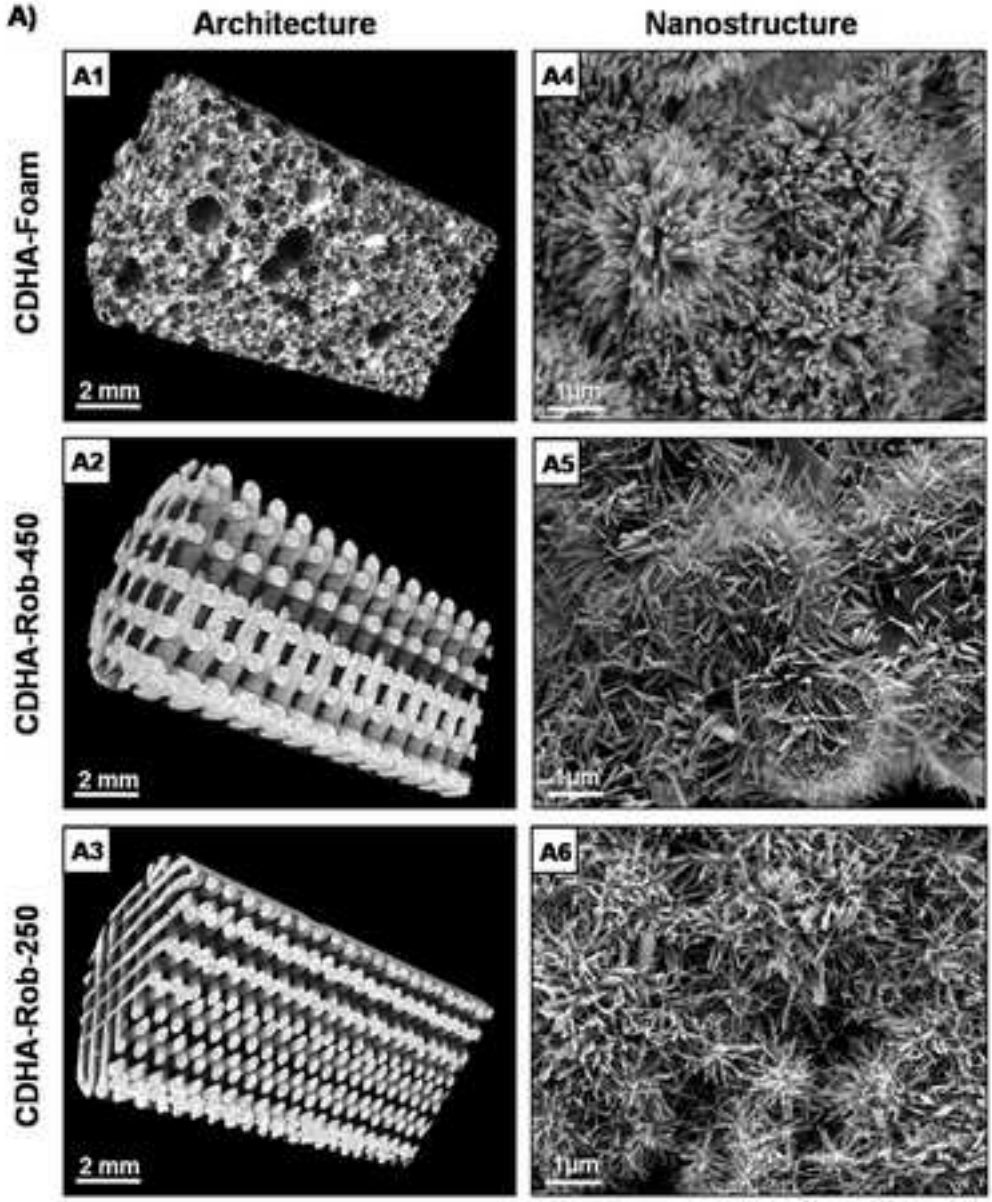

B) Porosity and SSA of the different scaffolds [Adapted from Barba et al 2017]

Materials	Porosity					SSA (m^2/g)
	% Total Porosity by MIP[a]	% Macroporosity by MIP[a]	% Macroporosity by micro-CT	Macropore entrance size by MIP (µm)[a]	Macropore size by micro-CT (µm)	
CDHA-Foam	76.5	49.5	52.3 ± 1.3[b]	70	227.0 ± 7.6[b]	38.49 ± 0.05[c]
CDHA-Rob-450	64.8	46.5	47.4 ± 0.9[b]	350	409.7 ± 5.4[b]	32.02 ± 0.03[c]
CDHA-Rob-250	65.4	48.7	54.1 ± 0.8[b]	200	288.7 ± 3.2[b]	32.35 ± 0.04[c]

[a] Results of one measurement with four specimens.

[b] and [c] No statistically significant differences were observed between materials ($p > 0.05$, n=4).

[d] Statistically significant differences were noted between materials ($p < 0.05$, n=4).

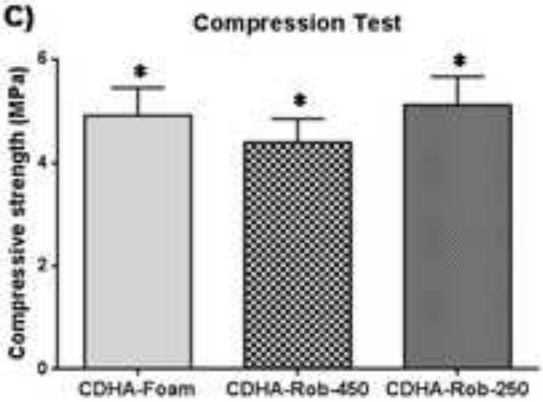

Figure(s)

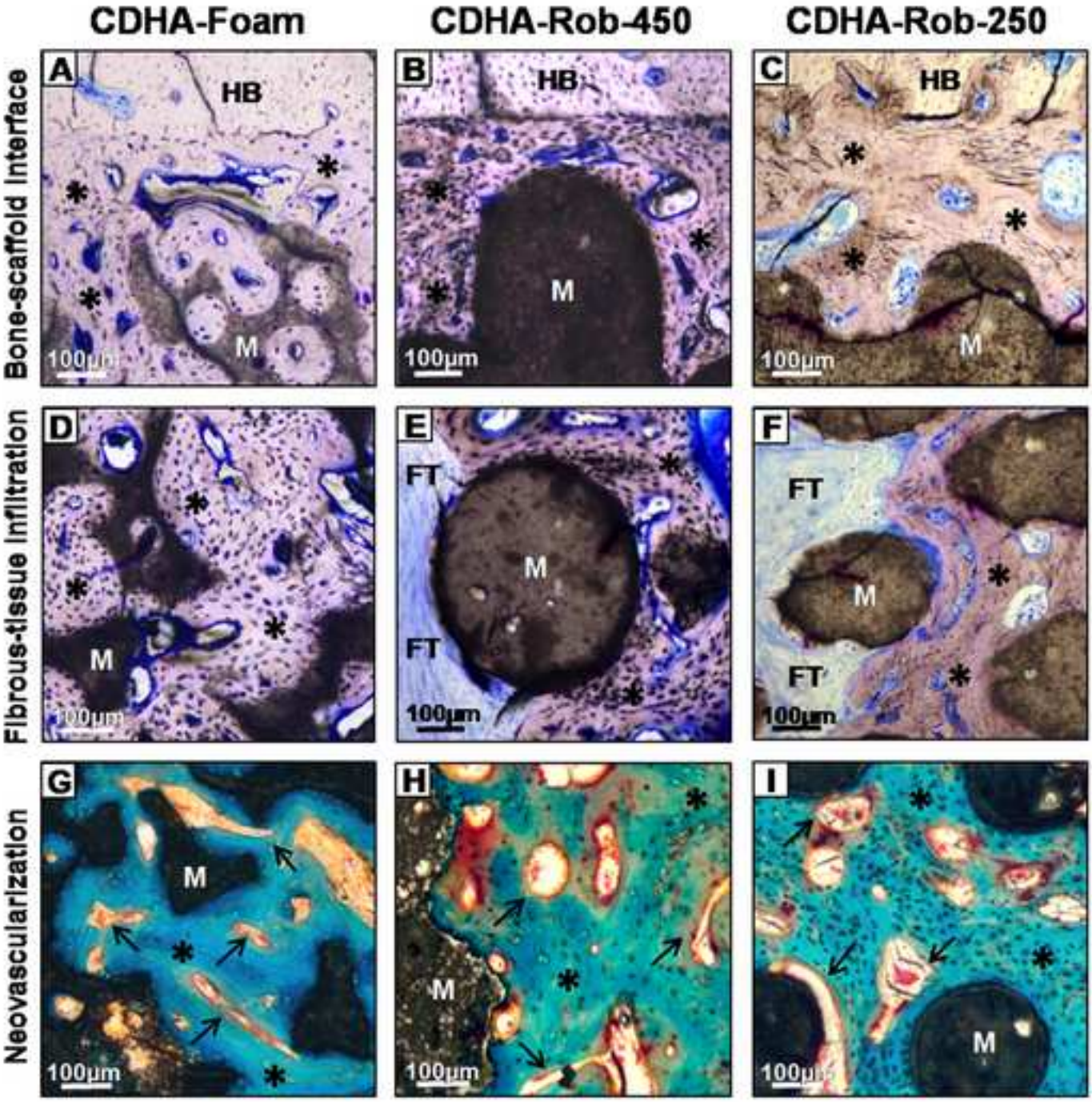

Figure(s)

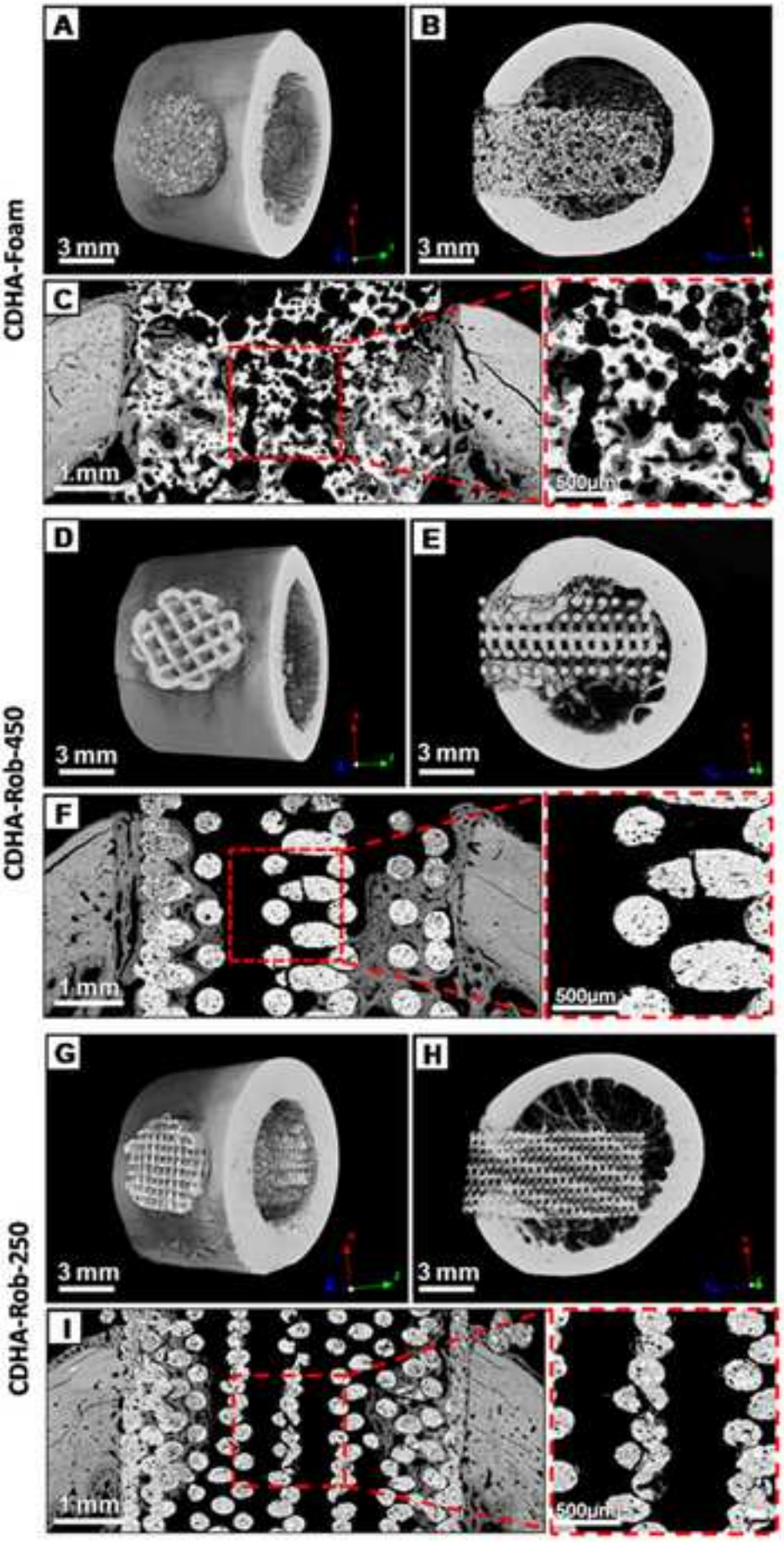

Figure(s)

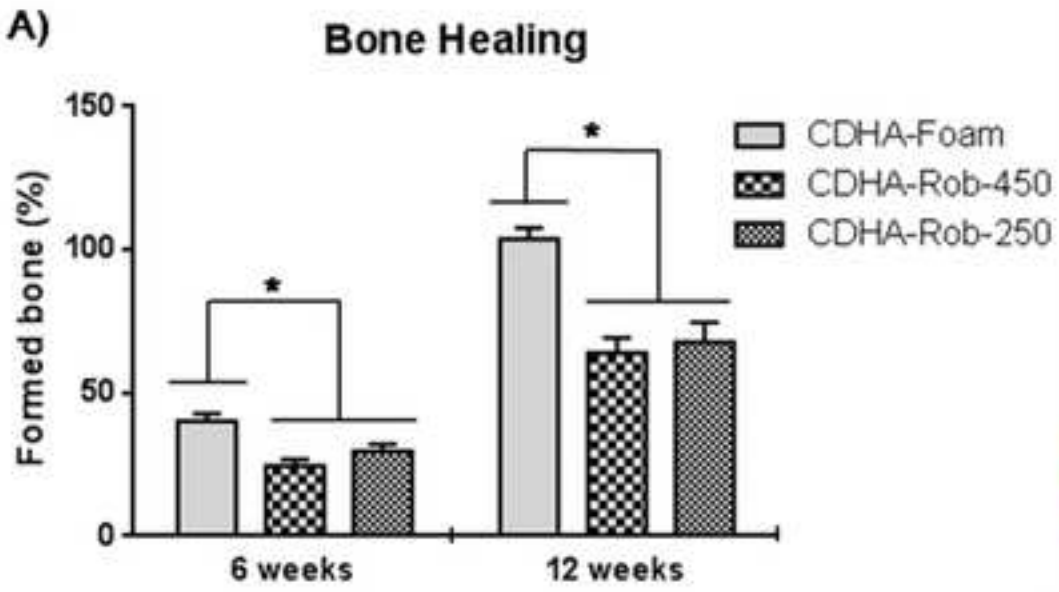

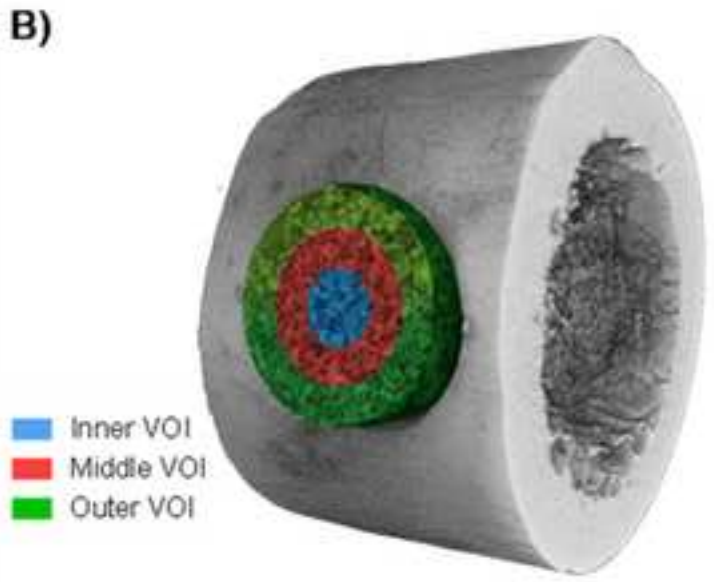

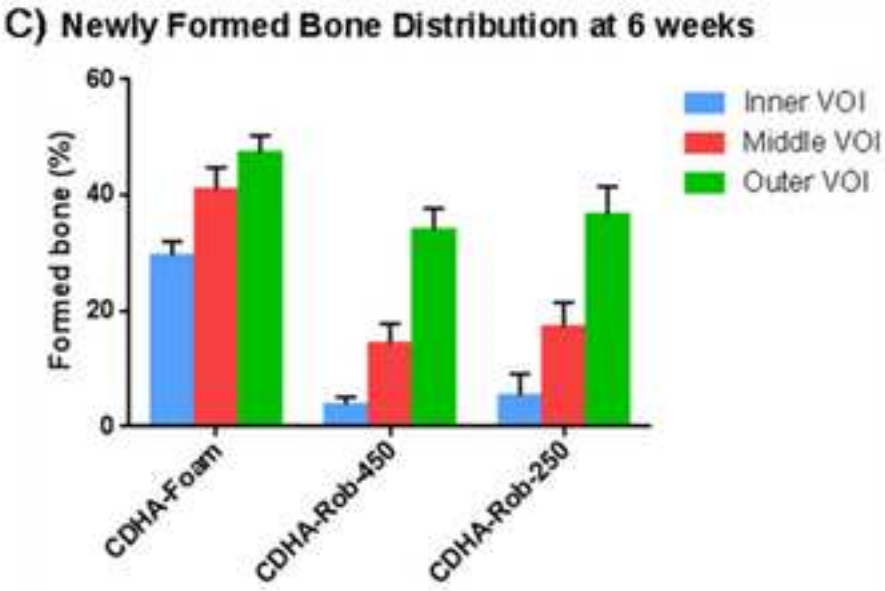

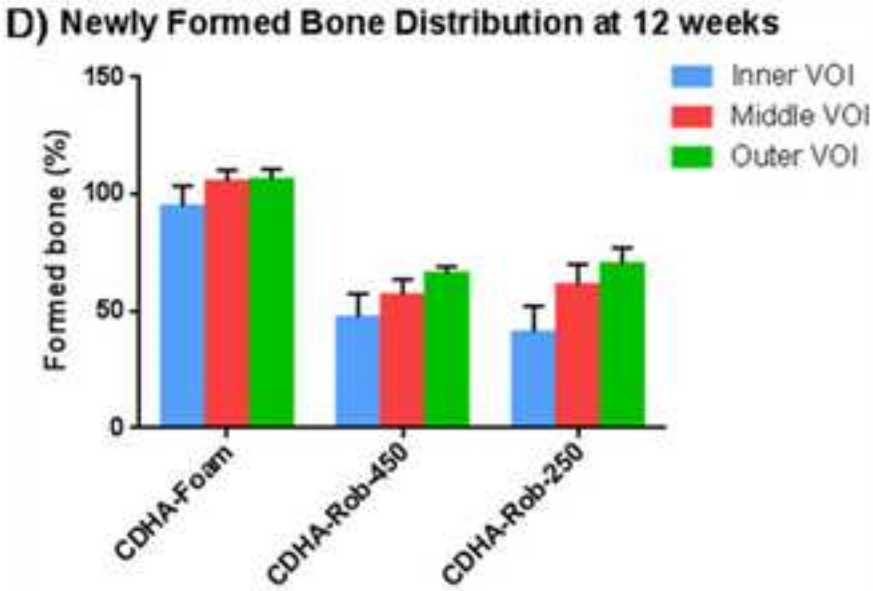

Figure(s)

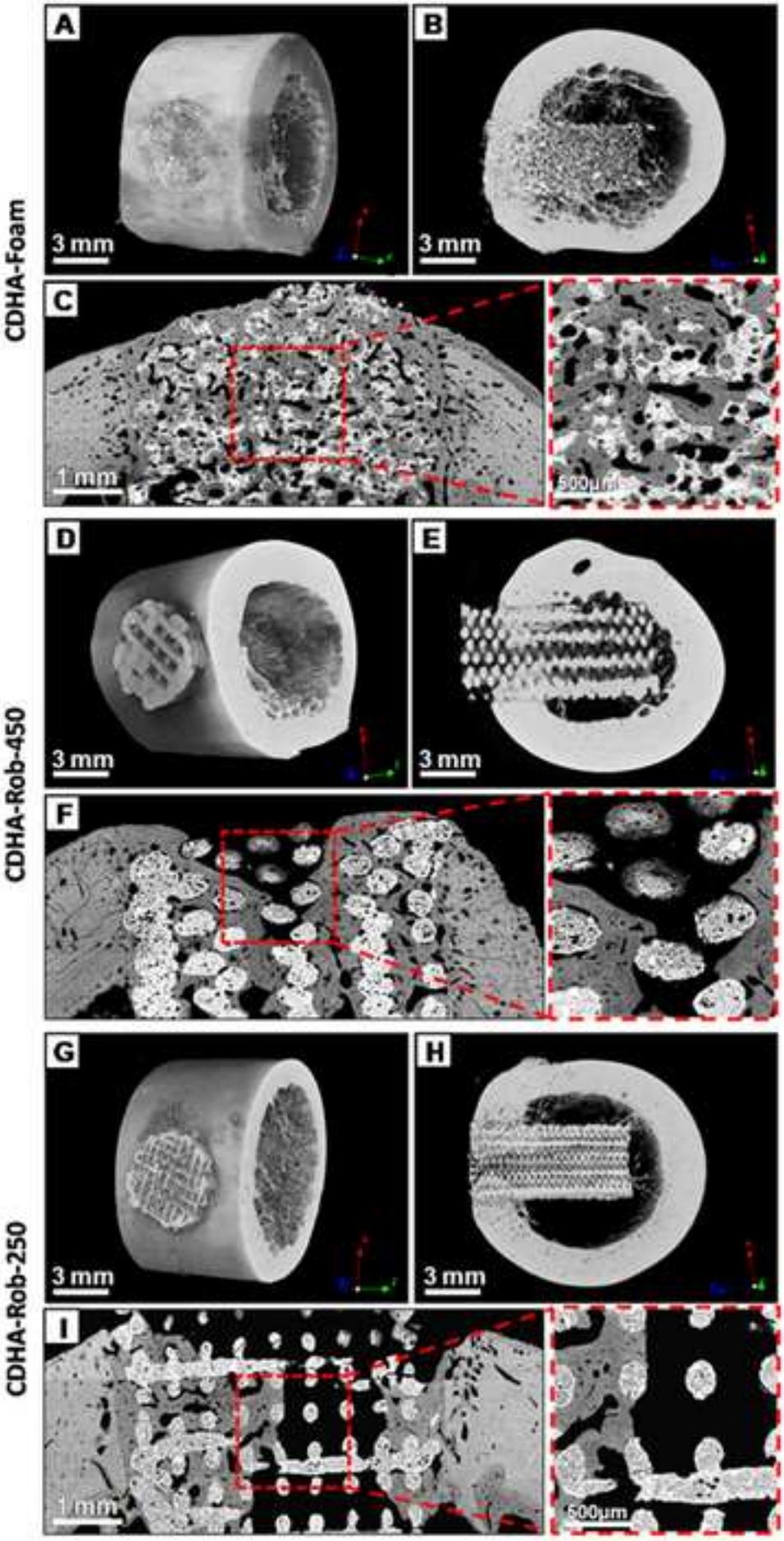

Figure(s)